Journal of Medicinal Chemistry

pubs.acs.org/jmc Article

Synthesis of Mitochondria-Anchored Nitroimidazoles with a Versatile NIR Fluorophore for Hypoxic Tumor-Targeting Imaging and Chemoradiotherapy

Sha Chen,[⊥] Songtao Yu,[⊥] Zaizhi Du, Xie Huang, Meng He, Shuang Long, Jing Liu, Yu Lan, Dong Yang, Hao Wang, Shuhui Li, An Chen, Yuhui Hao, Yongping Su, Changning Wang,* and Shenglin Luo*

Cite This: *J. Med. Chem.* 2021, 64, 3381−3391 Read Online

ACCESS | Metrics & More | Article Recommendations | Supporting Information

ABSTRACT: Nitroimidazoles are one of the most common radiosensitizers investigated to combat hypoxia-induced resistance to cancer radiotherapy. However, due to poor selectivity distinguishing cancer cells from normal cells, effective doses of radiosensitization are much closer to the doses of toxicity induced by nitroimidazoles, limiting their clinical application. In this work, a tumor-targeting near-infrared (NIR) cyanine dye (IR-808) was utilized as a targeting ligand and an NIR fluorophore tracer to chemically conjugate with different structures of hypoxia-affinic nitroimidazoles. One of the NIR fluorophore-conjugated nitroimidazoles (808-NM2) was identified to preferentially accumulate in hypoxic tumor cells, sensitively outline the tumor contour, and effectively inhibit tumor growth synergistically by chemotherapy and radiotherapy. More importantly, nitroimidazoles were successfully taken into cancer cell mitochondria via 808-NM2 conjugate to exert the synergistic effect of chemoradiotherapy. Regarding the important roles of mitochondria on cancer cell survival and metastasis under hypoxia, 808-NM2 may be hopeful to fight against hypoxic tumors.

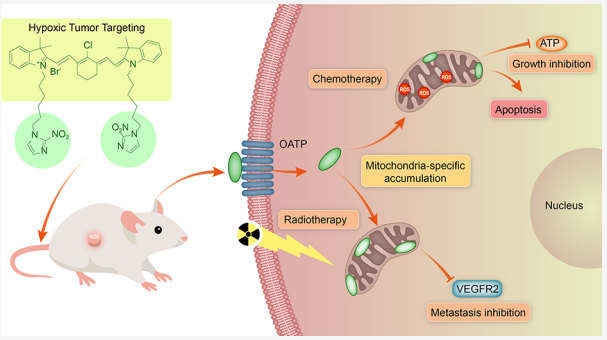

INTRODUCTION

Hypoxia is a cardinal component of the tumor microenvironment and plays a key role in tumor cell resistance to therapy, disease progression, and metastasis.[1] In particular, radiotherapy, as one of the main strategies for cancer treatment, is sensitively affected by hypoxia.[2] To combat the hypoxia-induced resistance to radiotherapy, several approaches have been pursued, including efforts to reoxygenate the tumor, radiosensitize hypoxic cells, and develop hypoxia-activated prodrugs.[3−7] A notable progress in clinic toward hypoxia-targeting cancer treatment was made by nitroimidazoles as oxygen-mimetic radiosensitizers.[8,9] In their structures, the electron-affinic nitro group is designed to react with DNA radicals produced by ionizing radiation in a manner similar to oxygen. The formation of these adducts leads to DNA strand breaks and subsequent cell death. However, due to the poor selectivity distinguishing cancer cells from normal cells, the effective doses of radiosensitization are much closer to those of the toxicity induced by nitroimidazoles, severely limiting their clinical application.[10]

In recent years, a series of structurally inherent tumor-targeting heptamethine indocyanine dyes, such as IR-808,[11] IR-780,[12] and IR-783,[13] have been discovered. These dyes exhibit near-infrared (NIR) fluorescence emission and preferential accumulation in tumor cells without ligand conjugation, providing potential applications for tumor diagnosis, drug delivery, and imaging-guided treatment. Into the tumor-targeted parent structure of IR-808, some radionuclides,[14,15] anticancer drugs,[16,17] and photosensitizers[18,19] were introduced and successfully used for tumor-specific multimodal imaging (NIR, positron emission tomography (PET), or single-photon emission computed tomography (SPECT)) and treatment (chemotherapy, photodynamic, or photothermal therapy). Although some conjugates exhibited excellent antitumor effects in both *in vitro* and *in vivo* studies, their treatment toward hypoxic tumors has not been tested. Hypoxic tumors are known to be more resistant to chemotherapy and radiotherapy, leading to poor prognosis and higher patient mortality.[1−3] The presence of hypoxic regions within tumors hinders the effect of both chemotherapy and radiotherapy.[20]

In this work, we designed and synthesized different covalent conjugations by introducing nitroimidazoles to the N-alkyl side chains of IR-808 dye based on previous structure−activity

Received: December 28, 2020
Published: March 10, 2021

https://dx.doi.org/10.1021/acs.jmedchem.0c02250
J. Med. Chem. 2021, 64, 3381−3391

Scheme 1. Structures and Synthetic Route of Different 808-Nitroimidazole Conjugates

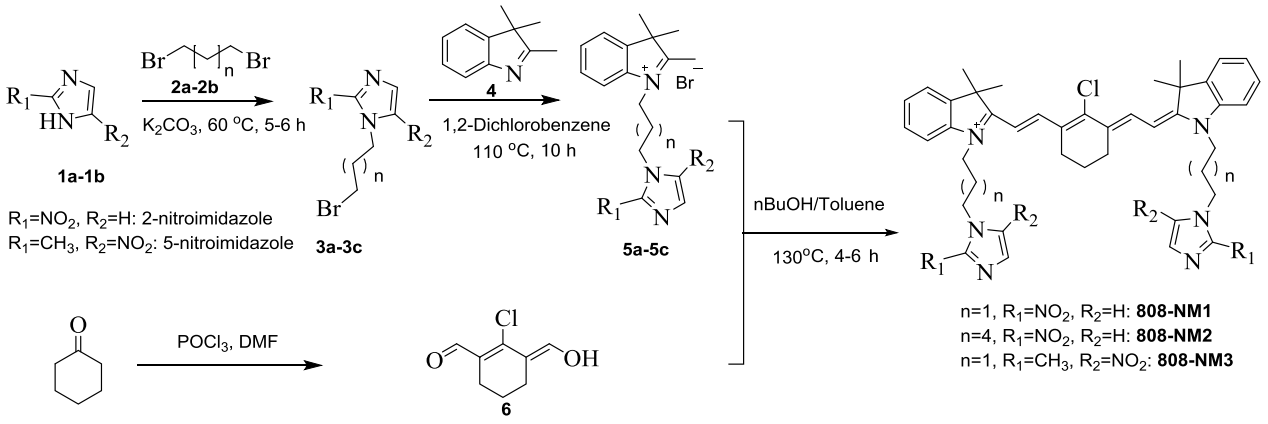

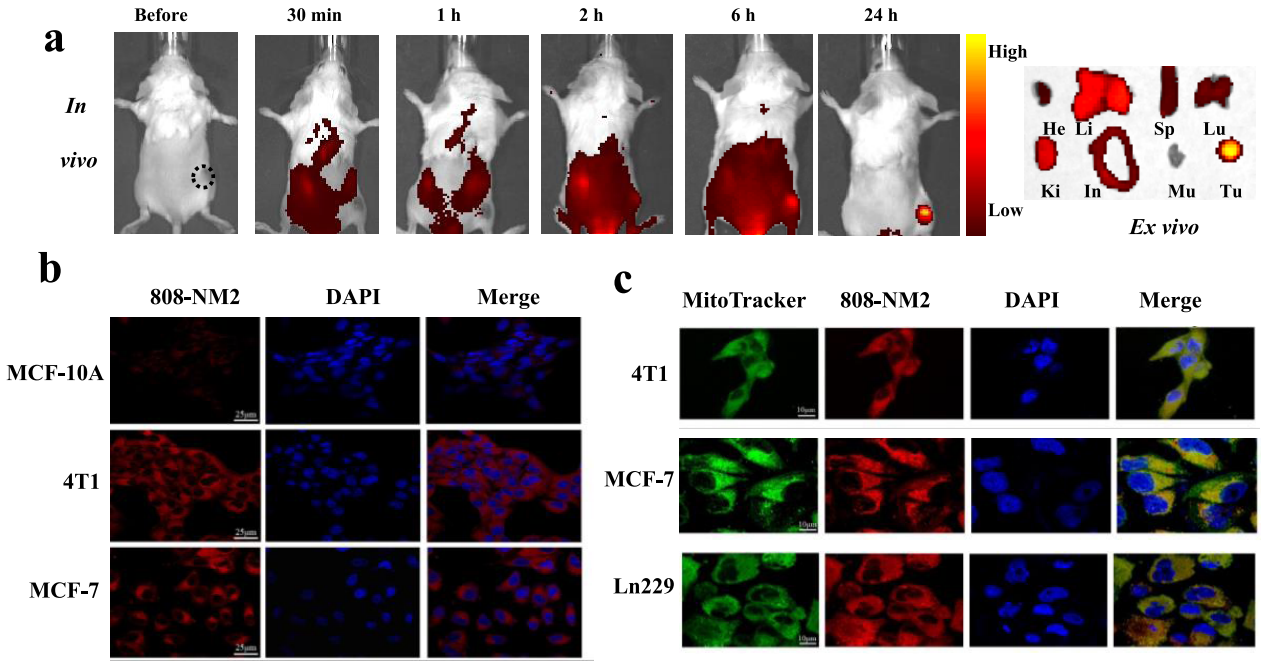

Figure 1. I*n vivo* and *in vitro* tumor-preferential accumulation of 808-NM2. (a) *In vivo* and *ex vivo* NIR fluorescent imaging of subcutaneous 4T1 tumor xenograft. The *ex vivo* imaging of dissected main organs (He: heart, Li: liver, Sp: spleen, Lu: lung, Ki: kidney, In: intestine, Mu: muscle, Tu: tumor) was performed 24 h after the injection of 808-NM2. (b) Confocal fluorescence microscope showed that 808-NM2 preferentially accumulated into cancer cells (4T1, MCF-7 cells) rather than normal cells (MCF-10A). (c) Intracellular localization of 808-NM2 (red) in three different kinds of cancer cells with mitochondria-specific probe MitoTracker (green).

relationship studies for tumor targeting.[21,22] Our results in this work showed that one of the 808-nitroimidazole conjugates (808-NM2) exhibited hypoxic cancer cell preferential uptake and effective growth inhibition due to a synergistic effect of chemotherapy and radiosensitization. Furthermore, the dual-modal therapeutic conjugate was specifically located in cancer cell mitochondria, which are the crucial cellular organelles for promoting cancer cell survival and metastasis in the hypoxic environment. Hence, the reported conjugate also showed to inhibit cancer cell migration or metastasis through *in vitro* and *in vivo* preliminary experiments. This new 808-nitroimidazole conjugate may present a versatile small molecule to integrate hypoxic cancer cell targeting, NIR imaging, chemoradiotherapy.

RESULTS AND DISCUSSION

As shown in Scheme 1, different 808-nitroimidazole conjugates were designed and chemically synthesized using 2-nitroimidazole or 5-nitroimidazole as the starting material. Their synthesis was not a straightforward conjugation between IR-808 and nitroimidazoles because there was no reactive chemical group available to directly link two structures. The synthetic routes and methods are also shown in detail in Figures S1 and S2. The successful synthesis of these conjugates was characterized by ^{1}H nuclear magnetic resonance (NMR), ^{13}C NMR, and high-resolution mass spectrometry (Figures S3 and S4). The purity of all final compounds was above 99% (Figure S5). Their optical spectra were determined and demonstrated both the maximal absorbance and emission in the NIR region (700−900 nm) with a high extinction coefficient (Figure S6 and Table S1).

With the NIR fluorescent property, the cancer-targeting ability of the three conjugates was evaluated on 4T1-bearing tumor xenografts (Figures 1a and S7). *In vivo* NIR imaging revealed that 808-NM2 exhibited tumor-preferential accumu-

https://dx.doi.org/10.1021/acs.jmedchem.0c02250
J. Med. Chem. 2021, 64, 3381−3391

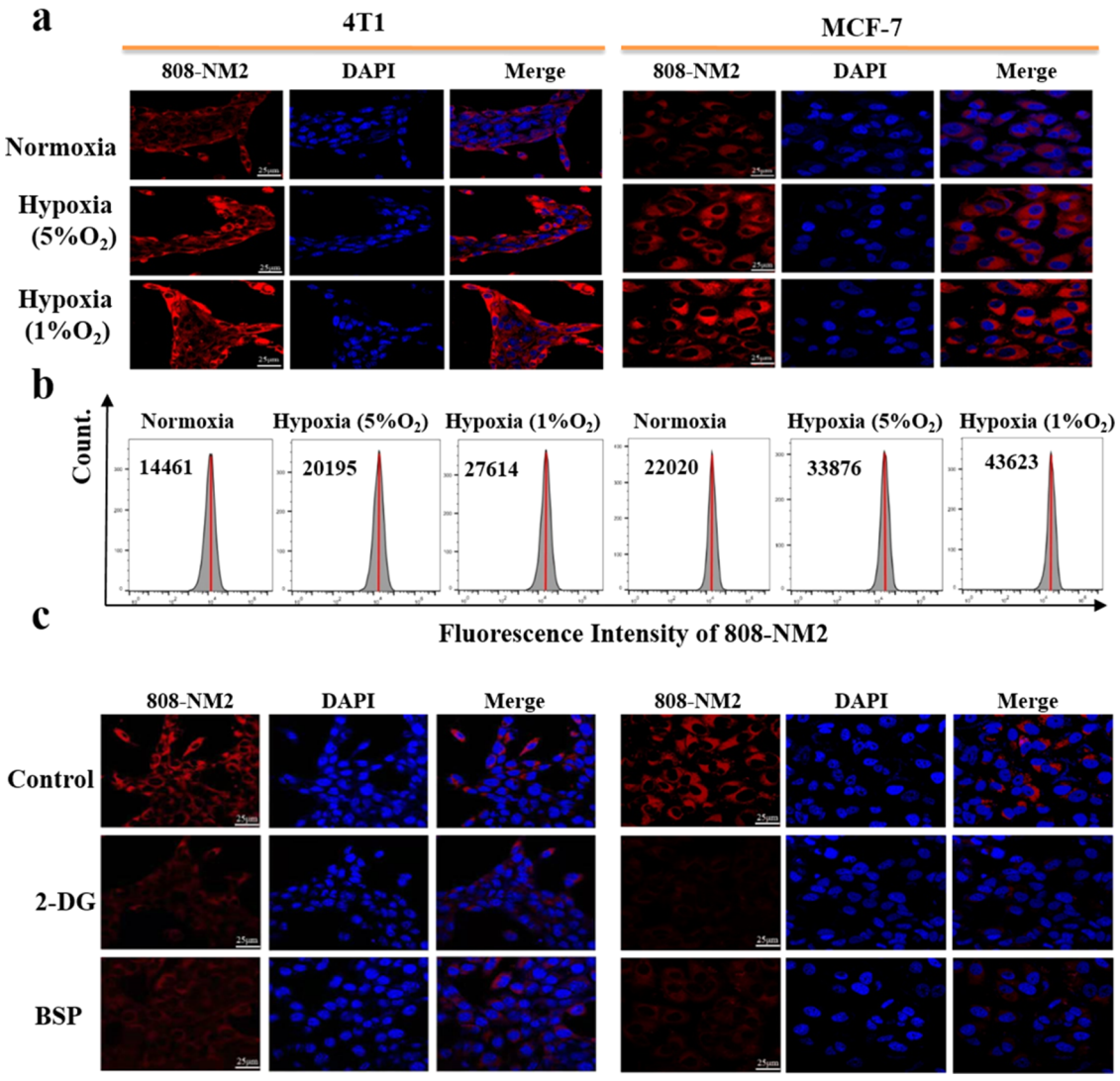

Figure 2. Hypoxia-induced increase in cancer cell uptake of 808-NM2 and mechanism studies. (a) Comparison of cell uptake under normoxic or hypoxic conditions (21, 5, 1% O_2) by the confocal fluorescent microscope images of 4T1 and MCF-7 cancer cells. (b) Comparison of cell uptake under normoxic or hypoxic conditions by flow cytometry and quantitative analysis (left three: 4T1; right three: MCF-7). (c) Mechanism studies of cellular uptake in tumor cells by the interventions of 2-DG and BSP pretreatment (left: 4T1; right: MCF-7).

lation at 24 h after injection. *Ex vivo* NIR imaging of the dissected organs and tumors further revealed that 808-NM2 preferentially accumulated in tumors. For *in vitro* tests, the uptake of 808-NM2 by 4T1 and MCF-7 cancer cells was investigated and compared with that of the normal epithelial cell line MCF-10A. Both fluorescence confocal images and flow cytometric results revealed preferential 808-NM2 accumulation in cancer cells (Figure 1b). Subcellular localization of 808-NM2 in 4T1, MCF-7, and Ln229 cancer cells (Figure 1c) further demonstrated its specific accumulation in mitochondria. Fluorescence confocal microscopy images showed that the red fluorescence of 808-NM2 overlapped with the green fluorescence of a mitochondrial tracker (MitoTracker) in all cancer cell lines, suggesting that the nitroimidazole moiety was successfully taken into mitochondria. Mitochondria are vital organelles for cell survival, providing energy production, and inducing apoptosis and autophagy.[23] In cancer, mitochondria play key roles in tumor cell proliferation, invasion, and metastasis.[24] Hence, the mitochondria-anchored conjugate may greatly enhance the radiosensitization effect of nitroimidazoles. The mechanism of mitochondria targeting may be ascribed to the heptamethine core with lipophilic cationic property in the structure of IR-808, according to previous structure−activity relationship studies.[18,21,22] Because 808-NM2 was synthesized by introducing nitroimidazoles to the N-alkyl side chains of IR-808, the conjugation didn't change the heptamethine core and lipophilic cationic property. Hence, 808-NM2 remained to have the capacity of mitochondrial targeting accumulation.

Then, we investigated the cellular uptake of 808-NM2 under hypoxic conditions. After exposure to different hypoxic conditions (5% O_2, 1% O_2), cell uptake of 808-NM2 in both 4T1 and MCF-7 cancer cells was found to notably increase, compared to that under normoxic condition (21% O_2) (Figures 2a and S8). Flow cytometric analysis also quantitively confirmed the results in both cancer cell lines (Figure 2b). To further investigate the factors affecting cellular uptake of 808-NM2, cancer cells were treated with a glycolysis inhibitor 2-deoxy-D-glucose (2-DG). Results showed that glycolysis inhibitor 2-DG significantly decreased the cellular uptake of 808-NM2 (Figure 2c), suggesting that glycolysis may play an important role in the 808-NM2 uptake. Therefore, the possible mechanism of hypoxic

https://dx.doi.org/10.1021/acs.jmedchem.0c02250
J. Med. Chem. 2021, 64, 3381−3391

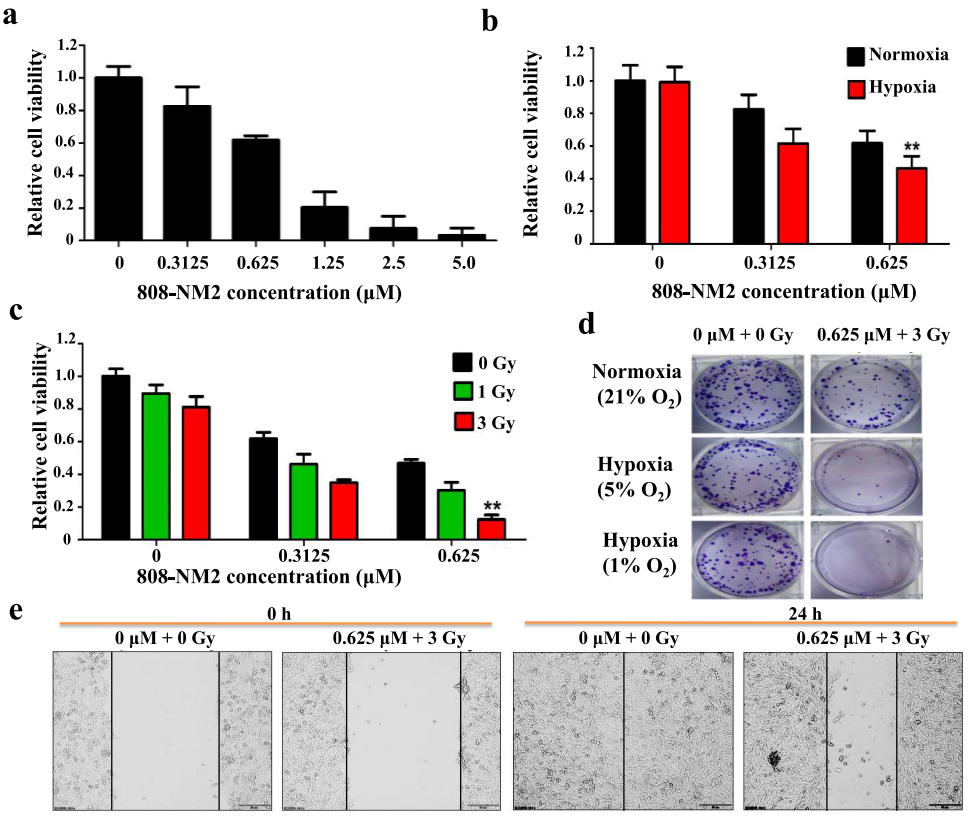

Figure 3. Growth and migration inhibition on hypoxic 4T1 tumor cells. (a) Relative cell viability of 4T1 cells detected by MTT 72 h after incubation with different concentrations of 808-NM2 under normoxic condition (21% O_2). (b) Relative cell viability of 4T1 cells 72 h after incubation with low concentrations of 808-NM2 under normoxic or hypoxic condition (21, 5% O_2). (c) Relative cell viability of 4T1 cells 72 h after a combined treatment with 808-NM2 and ionizing radiation under hypoxic condition (5% O_2). The results were expressed as the mean ± SD $^{**}p < 0.01$, $n = 6$, compared to the close-left group, respectively. (d) Clonogenic survival assay of 4T1 cells after different treatments at different oxygen levels (21, 5, 1% O_2). (e) Wound healing assay of 4T1 cells under hypoxia (5% O_2) before (0 h) or after different treatments (24 h).

cancer cell uptake of 808-NM2 may be associated with glycolysis metabolic pathway, which is similar to the previous reports of tumor-targeting IR-808.[25,26] In addition, the cellular uptake of 808-NM2 was also remarkably inhibited when preincubated with sulfobromophthalein (BSP), a competitive inhibitor of organic anion transporting polypeptide (OATP) transporters.[27] Because of the higher expression of OATP protein on cancer cells (MCF-7) over normal human cells (MCF-10A), the significant difference of 808-NM2 uptake between MCF-10A and MCF-7 cells indicated that OATP transporters either involved in one of the cancer-targeting mechanisms of 808-NM2.[11]

The inherent antiproliferative activity of 808-NM2 was initially evaluated in cancer cells without ionizing radiation. MTT assays demonstrated that the cell viability of 4T1 cells gradually decreased with increasing concentrations (Figure 3a). For example, cell viability was reduced to 10% after 72 h incubation with 2.5 μM 808-NM2. Its antiproliferative effect was also confirmed in MCF-7, A549, and Ln229 cancer cells (Figure S9), indicating potent anticancer activity on a broad spectrum of cancer cells. Notably, its anticancer activity was dramatically enhanced when cells were incubated under hypoxic conditions (Figure 3b). This result is possibly induced by more efficient cellular uptake of 808-NM2 under hypoxic conditions. To better observe the effect of radiosensitization, low concentrations (0–0.625 μM) of 808-NM2 were incubated for 6 h under hypoxia followed by ionizing radiation. It could be easily found that cell viability at each concentration was gradually reduced when ionizing radiation was applied from 1 to 3 Gy (Figures 3c and S10). Specifically, nearly no cell viability was found after co-treatment with 0.6250 μM 808-NM2 plus 3 Gy radiation under hypoxia (1% O_2, Figure S11). The results revealed that a remarkable anticancer effect was obtained by a combination of chemotherapy and radiosensitizing effect. The number and morphology of cancer cells after the treatment also visually illustrated the synergistic effect of chemotherapy and radiotherapy (Figure S12). A clonogenic survival assay was performed, as it is known as the "gold standard" to assess the radiosensitizing effect of a radiosensitizer.[28,29] The photographs shown in Figures 3d and S13 intuitively demonstrate that colony formation was almost completely inhibited under hypoxia compared with normoxia, suggesting that 808-NM2 could act as a radiosensitizer with a good radiosensitizing effect. As mentioned before, hypoxia plays an important role in cancer cell metastasis. The inhibition of cell migration was evaluated by wound healing assays with cancer cells. As shown in Figure 3e, cell migration was obviously inhibited by the 808-NM2-treated ionizing radiation group under hypoxia, which was much more effective than that under normoxia (Figure S14). This tendency was also verified in MCF-7 cancer cells (Figure S15).

For the anticancer mechanism study, the mitochondrial membrane potential was detected by flow cytometry with the mitochondria-targeted probe rhodamine 123.[30] The average fluorescence intensity of Rho123 decreased remarkably after ionizing radiation with 0.625 μM 808-NM2 (Figure S16), indicating that the mitochondrial membrane potential was

https://dx.doi.org/10.1021/acs.jmedchem.0c02250
J. Med. Chem. 2021, 64, 3381−3391

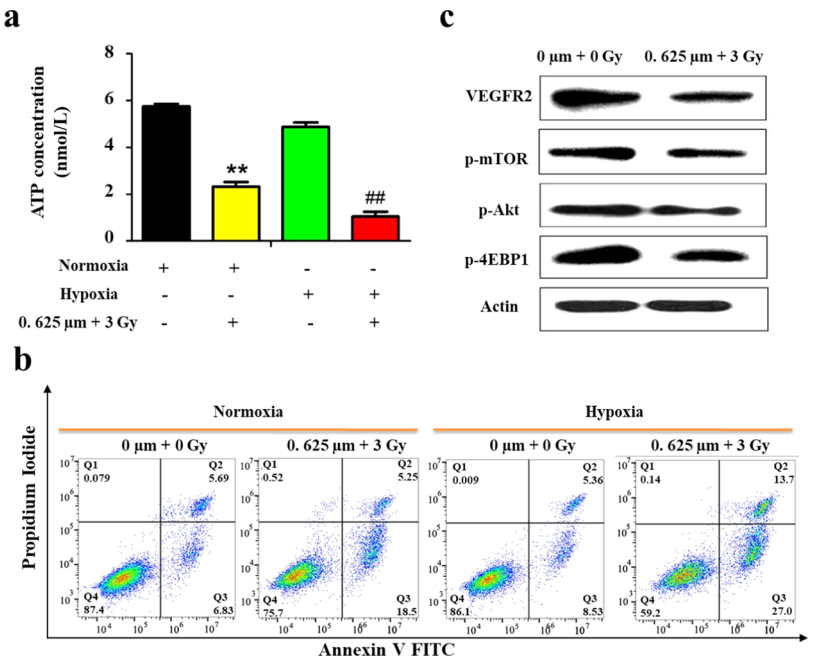

Figure 4. Anticancer mechanism of 808-NM2 on hypoxia tumor cells. (a) Detection of ATP in 4T1 cells 72 h after different treatments. The results were expressed as the mean ± SD, $^{**}p < 0.01$, compared to normoxia control; $^{\#\#}p < 0.01$, compared to hypoxia control, $n = 3$. (b) Apoptosis assay of 4T1 cells by flow cytometry 24 h after different treatments. (c) Expression of VEGFR2, p-mTOR, p-Akt, and p-4EBP1 in 4T1 cells 72 h after different treatments. Normoxia and hypoxia indicate 21, 5% O_2, respectively.

severely affected. Second, the production of ATP was detected and found to be significantly reduced in the 808-NM2 radiation group (Figure 4a). Third, ionizing radiation-induced radicals, specifically reactive oxygen species (ROS), in mitochondria were determined and revealed that much more ROS in mitochondria were produced in the 808-NM2 ionizing radiation group than in the control (Figure S17). These hyperactive ROS may attack mitochondrial DNA (mtDNA) and perturb mitochondrial functions for growth and migration.[31] It is also well known that high ROS generation and severe damage to the mitochondrial membrane potential easily trigger the apoptosis pathway of cell death.[32] Indeed, both early and late apoptosis were increased after the combined treatment under hypoxia (Figures 4b and S18). Furthermore, we found that vascular endothelial growth factor receptor 2 (VEGFR2) protein expression decreased after treatment (Figure 4c). VEGFR2 is a predominant inducer of both normal and pathophysiological angiogenesis. It is activated by the hypoxic response elements within the VEGF gene promoter.[33] In addition, there was a sharp decrease in the expression of p-mTOR, p-Akt, and p-4EBP1 (Figures 4c and S19), which are the key proteins in the PI3K/AKT/mTOR signaling pathway regulating cell growth, cell cycle progression, and angiogenesis.[34] These findings may provide possible mechanisms not only for tumor growth inhibition but also for metastasis suppression induced by mitochondria-targeted 808-NM2.

The *in vivo* antitumor efficacy of 808-NM2 was initially elucidated in an aggressive 4T1 subcutaneous tumor xenograft mouse model. After the tumors reached 100 mm^3, all mice were randomly divided into three groups: the blank control group, the 808-NM2 group, and the 808-NM2 combined with the ionizing radiation group. According to the *in vivo* NIR imaging results, 808-NM2 preferentially accumulated in tumors 24 h after injection and 4 Gy ionizing radiation was given to tumors 24 h after the injection of 808-NM2 via mouse tail veins (Figure S20, repeated three times of ionizing radiation with a total dose of 12 Gy). The tumor growth curves showed that tumor growth was arrested in the 808-NM2-treated group and significantly suppressed in the 808-NM2 irradiation group (Figure 5a). The mean tumor weight in the 808-NM2 irradiation group was much less than that in the 808-NM2 alone group (Figure 5b,c). The number of tumor nodules on each lung was counted under a microscope and obviously decreased in the mice from the 808-NM2-treated radiation group (Figure 5d). H&E staining of the lungs showed that a great number of tumor cells had migrated into lung organs in the control and 808-treated groups but not in the 808-NM2 radiation group (Figure 5e). Tumor tissues were routinely processed and immunohistochemically stained for CD31 and CD34, which are well known as markers for benign and malignant vascular tumors.[35] The results revealed that the expression of both proteins was obviously decreased in the 808-NM2-treated radiation group compared with the control group (Figure S21). Therefore, both *in vitro* and *in vivo* results reveal that 808-NM2 has a synergistic antiproliferative and radiosensitization effect on tumor growth inhibition.

Finally, to explore the potential for translational applications, the *in vivo* antitumor efficacy of 808-NM2 was further evaluated in a patient-derived xenograft (PDX) mouse model. Cancer specimens derived from clinical patients were collected, and patient diagnostic characteristics are shown in Table S2. 808-NM2 was intravenously injected into mice in the PDX model group and sham-operated group. *In vivo* NIR fluorescent imaging of the anesthetized mice at 24 h postinjection showed that an intensive fluorescent signal was observed at the tumor-implanted site rather than at the sham-operated site (Figure 6a), indicating that 808-NM2 maintained preferential tumor accumulation in the PDX model. Then, 4 Gy ionizing radiation was given to patient-derived xenografts and repeated three times with a total dose of 12 Gy. Tumor growth was inhibited significantly in the 808-NM2-treated nonradiation group based

https://dx.doi.org/10.1021/acs.jmedchem.0c02250
J. Med. Chem. 2021, 64, 3381−3391

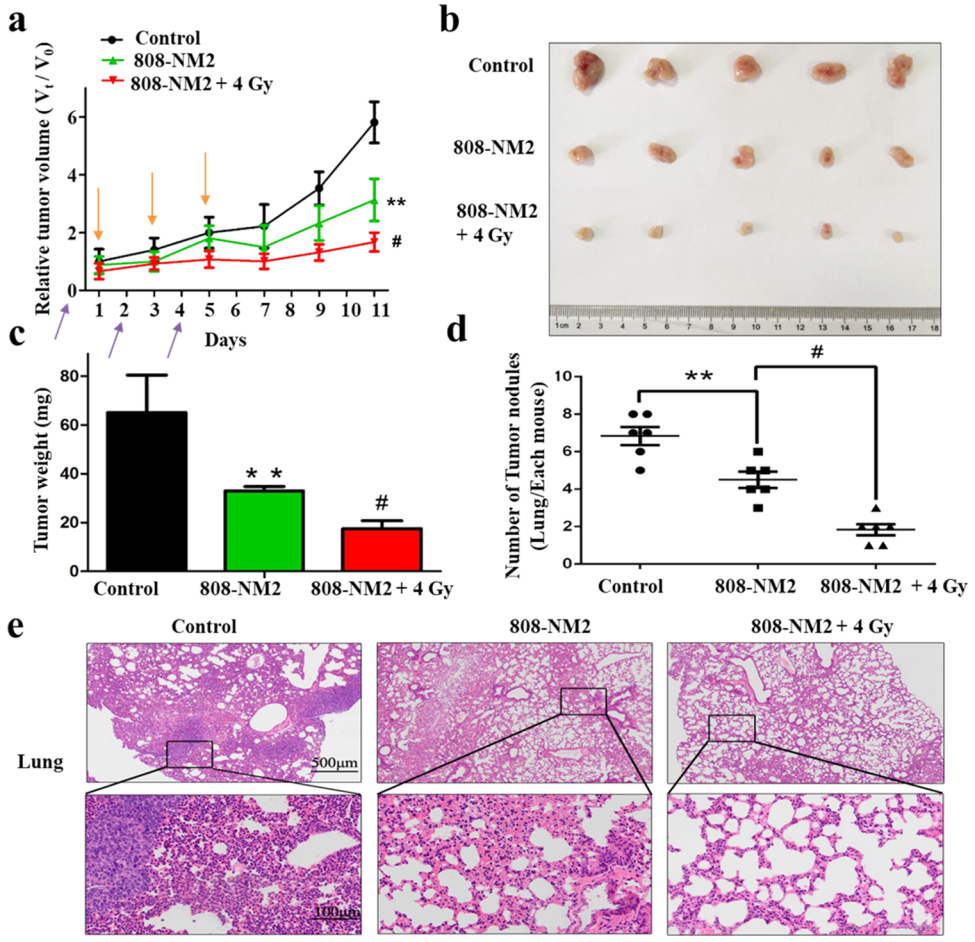

Figure 5. *In vivo* anticancer effect on metastatic 4T1 subcutaneous tumor models. (a) Tumor growth curves of 4T1 tumor xenograft mice in different groups were measured during the observation period. Purple and orange arrows indicate the days of drug injection or ionizing radiation, respectively. $^{**}p < 0.01$, compared to control; $^{\#}p < 0.05$, compared to 808-NM2 group, $n = 6$. (b) Photos of tumors dissected from 4T1 tumor xenograft mice. (c) Tumor weight in different groups. (d) Number of tumor nodules in mouse lungs from different groups was counted by a microscope. (e) H&E staining of lung (dark blue spots) from different groups for pathological histology analysis. The group of 808-NM2+4 Gy means three 4 Gy doses of ionizing radiation for a total dose of 12 Gy.

on the tumor growth curves and the mean tumor weight (Figure 6b,c, compared to the control group). The inhibition was further enhanced in the 808-NM2 combined irradiation group (compared to the 808-NM2 group). The body weight of mice was monitored during treatment, and no significant differences among groups were observed, suggesting good tolerance of all of the treatments (Figure 6d). Mice were sacrificed, and the tumors grown from cancer specimens were retrieved at the end of the observation period. The tumor tissues were immunohistochemically stained for CD31 and CD34 (Figure S22). Both results demonstrated that they underwent a dramatic decrease in the 808-NM2 radiation group. The tumor tissues were further subjected to Ki67 (Figure 6e) and VEGFR2 immunochemical staining (Figure S23). The results showed that the expression of all of these genes decreased after treatment, indicating a potential antimetastatic effect by inhibiting tumor angiogenesis.

CONCLUSIONS

In summary, a multifunctional NIR fluorophore was developed for preferential accumulation in hypoxic cancer cells, sensitive NIR fluorescence imaging, effective tumor growth, and metastasis inhibition synergistically by chemoradiotherapy. This versatile NIR fluorophore, namely, 808-NM2, was synthesized and screened out from different covalent conjugates by introducing hypoxia-affinic nitroimidazoles into IR-808 as a novel tumor-targeting ligand. First, 808-NM2 retained the property of preferential tumor accumulation mediated by OATP transporters, which are overexpressed in a variety of cancer cells. Second, this new 808-nitroimidazole conjugate with two nitroimidazole groups exhibited a hypoxia-induced increase in cancer cell uptake. Third, it could exert a synergistic anticancer effect of chemotherapeutic and radiosensitizing activities, possibly due to a hypoxia-induced increase in cell uptake by cancer cells. More noteworthy, 808-NM2 was found to be specifically retained in cancer cell mitochondria, disrupted mitochondrial function and energy production and remarkably decreased the adaptation of cancer cells to hypoxic environments to sensitize the anticancer effect of ionizing radiation. This 808-nitroimidazole conjugate reported in this work, with simultaneous hypoxia-enhanced cancer cell uptake and multimodal therapeutic activities by targeting mitochondria, may present a useful strategy to combat hypoxia-induced cancer therapy resistance.

EXPERIMENTAL SECTION

Chemicals and Instruments. Chemicals and solvents used for synthesis were purchased from commercial suppliers (Sigma-Aldrich or Acros) and directly used without further purification. All reactions were

https://dx.doi.org/10.1021/acs.jmedchem.0c02250
J. Med. Chem. 2021, 64, 3381−3391

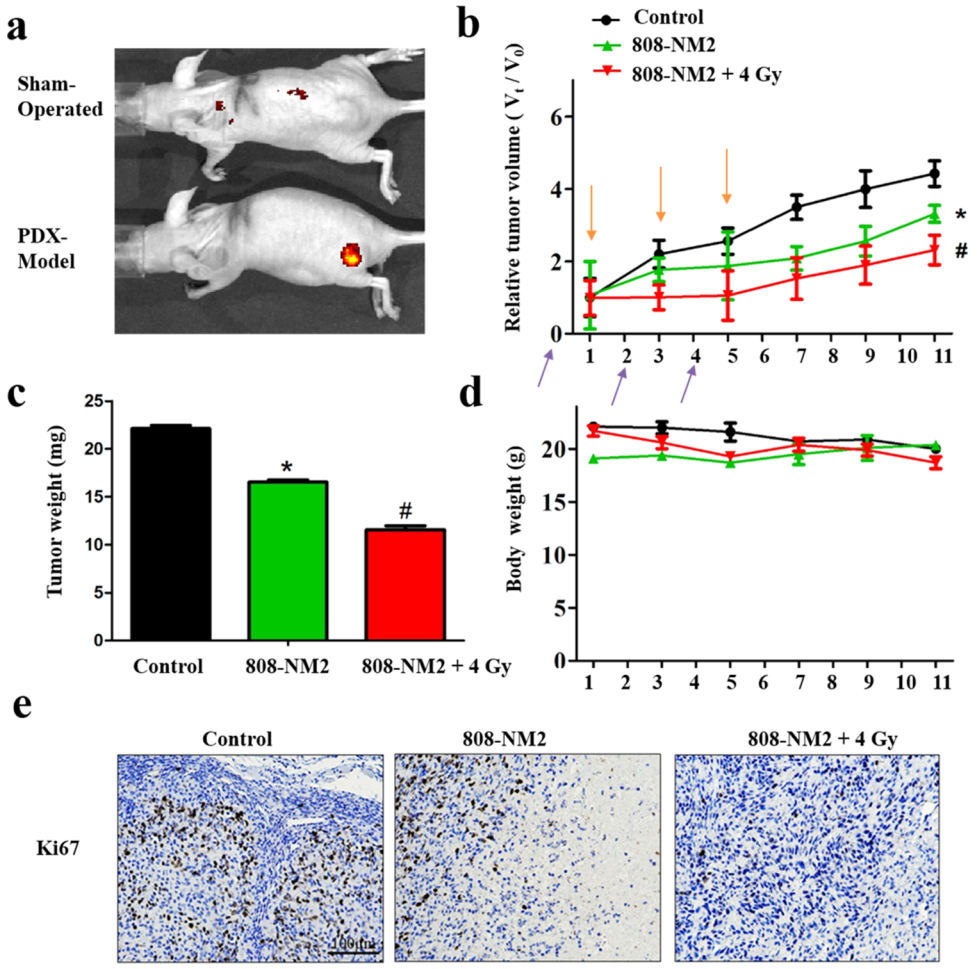

Figure 6. *In vivo* anticancer effect on patient-derived xenografts. (a) *In vivo* NIR imaging of mice from the sham-operated group and PDX model group 24 h after the injection of 808-NM2. (b) Tumor growth curves in the PDX mouse model in different groups during the observation period. Purple and orange arrows indicate the days of drug injection or ionizing radiation, respectively. $^{\#}p < 0.01$, $^{*}p < 0.05$, compared to control, $n = 3$. (c) Tumor weight in different groups. (d) Body weight of mice from different groups after treatment. (e) Immunohistochemical staining of Ki67 (dark brown spots) in tumor sections from different treatment groups. The group of 808-NM2+4 Gy means three 4 Gy doses of ionizing radiation for a total dose of 12 Gy.

monitored by thin-layer chromatography (TLC). Flash chromatography was carried out using silica gel (300−400 mesh). ^{1}H NMR spectra were recorded with a Varian 400 MHz with trimethylchlorosilane (TMS) as an internal standard. High-resolution mass spectrometry (HRMS) was performed on a Bruker BioTOF IIIQ system. NIR spectroscopy was performed using an NIR spectrophotometer (Shimadzu, UV-3600). Photoluminescence was determined with 740 nm excitation and scanning the wavelength from 750 to 900 nm using an NIR fluorescence spectrometer (Lumina Fluorescence Spectrometer, Thermo Fisher USA). The purity of the final compounds was determined by high-performance liquid chromatography (HPLC). The purity of all final compounds was 95% or higher. The instrument was a Shimadzu LC-6A with two pumps (LC-6AD) and a UV−VIS detector (SPD-20AV). The column was Inertsil ODS-SP C18, 5 μm, 4.6 × 150 mm^2. Eluent A was CH_3CN, 0.1% TFA; eluent B was H_2O, 0.1% trifluoroacetic acid (TFA); flow rate was 1 mL/min, gradual eluent A from 0 to 95% for 11 min. The column temperature was room temperature.

Synthesis of 3a−3c. To a mixture of 2-nitroimidazole or 5-nitro-2-methyl-imidazole (20 mmol) and potassium carbonate (20 mmol, 2.76 g) in 15 mL of anhydrous dimethylformamide (DMF) was added 1,3-dibromopropane (2 mmol, 400 mg for **3a** or **3c**) or 1,6-dibromohexane (2 mmol, 484 mg, for **3b**) and then stirred at 60 °C until TLC monitoring was completed. The mixture was then diluted with 100 mL of ethyl acetate and washed with water (20 mL × 3) as well as brine (20 mL × 3). The organic layer was dried by anhydrous sodium sulfate and filtered. The filtration was concentrated, and the residue was purified by flash chromatography (EtOAc/hexane: 1/2) to give a white solid of **3a** (1.77 g, yield 38%), ^{1}H NMR δ 7.203 (d, J = 8.0 Hz, 1H), 7.185 (d, J = 8.0 Hz, 1H), 4.613 (t, J = 8.0 Hz, 2H), 3.360 (t, J = 8.0 Hz, 2H), 2.406 (m, J = 8.0 Hz, 2H). **3b** (2.59 g, yield 47%), ^{1}H NMR δ 7.133 (d, J = 4.0 Hz, 1H), 7.079 (d, J = 4.0 Hz, 1H), 4.404 (t, J = 8.0 Hz, 2H), 3.389 (t, J = 8.0 Hz, 2H), 1.889−1.354 (m, 8H). **3c** (3.06 g, yield 62%), ^{1}H NMR δ 7.724 (d, J = 8.0 Hz, 1H), 4.142 (t, J = 8.0 Hz, 2H), 3.381 (t, J = 8.0 Hz, 2H), and 2.462 (s, 3H), 2.327−2.305 (m, 2H).

Synthesis of 5a−5c. 2,2,3-Trimethyl-3H-indolenine (30 mmol) and different bromo-substituted nitroimidazole compounds (30 mmol) were mixed in 1,2-dichlorobenzene (15 mL) and stirred at 110 °C under argon protection for 10−12 h. The reaction mixture was cooled to room temperature and added to acetone. The brown precipitate or oil was collected and washed with acetone. Indolenine quaternary ammonium salts **5a−5c** were obtained and directly used in this next reaction without further purification.

Synthesis of 808-Nitroimidazole Conjugates. Quaternary ammonium salts **5a**, **5b** or **5c** (7.1 mmol) were mixed with **6** (3.3 mmol) in toluene/*n*-butanol [7:3 (v/v), 100 mL]. The mixture was heated under reflux for 4−6 h. After completion of the reaction, toluene and *n*-butanol were evaporated under reduced pressure to yield a yellow green solid. The crude material was dissolved in chloroform (50 mL) and precipitated with excess ether (150 mL). Further purification was performed with column chromatography using dichloromethane/methanol (15:1) as the eluent. Eventually, a green powder of each 808-

https://dx.doi.org/10.1021/acs.jmedchem.0c02250
J. Med. Chem. 2021, 64, 3381−3391

nitroimidazole conjugate was obtained. **808-NM1** (0.50 g, yield 18%, HPLC purity analysis 99.3%). ^{1}H NMR (400 Hz, $CDCl_3$): 8.25 (d, J = 8.0 Hz, 2H); 7.74 (S, 2H); 7.62 (d, J = 8.0 Hz, 2H); 7.45−7.42 (m, 4H); 7.27 (t, J = 4.0 Hz, 2H); 7.19 (s, 2H); 6.24 (d, J = 12.0 Hz, 2H); 4.53 (t, J = 4.0 Hz, 4H); 4.31 (J = 4.0 Hz, 4H); 2.65 (t, J = 4.0 Hz, 4H); 2.28−2.25 (m, 4H), 1.84−1.83 (m, 2H); and 1.66 (s, 12H). ^{13}C NMR (100 Hz, dimethyl sulfoxide (DMSO)-d_6): 172.74, 148.71, 145.07, 143.63, 142.38, 141.50, 129.05, 128.48, 127.89, 126.92, 125.71, 123.03, 111.76, 102.08, 49.51, 47.22, 41.55, 28.34, 27.91, 26.27, 21.50, and 20.78. HRMS $[M - Br]^+$: calculated 761.3325, found 761.3354. **808-NM2** (0.79 g, yield 26%, HPLC purity analysis 99.4%). ^{1}H NMR (400 Hz, $CDCl_3$): 8.22 (d, J = 8.0 Hz, 2H); 7.67 (s, 2H); 7.61 (d, J = 2 Hz, 2H); 7.43−7.40 (m, 4H); 7.27−7.25 (m, 2H); 7.15 (s, 2H); 7.29 (d, J = 6.0 Hz, 2H); 4.34 (t, J = 8.0 Hz, 4H); 4.18 (t, J = 4.0 Hz, 4H); 2.66 (t, J = 4.0 Hz, 4H); 1.83−1.82 (m, 2H); 1.76−1.69 (m, 8H); 1.64 (s, 12H); 1.42−1.39 (m, 4H); and 1.33−1.30 (m, 4H). ^{13}C NMR (100 Hz, DMSO-d_6): 172.60, 148.41, 144.96, 143.41, 142.49, 141.50, 129.06, 128.29, 128.27, 126.57, 125.61, 122.98, 111.97, 102.01, 49.75, 49.44, 44.17, 30.06, 27.91, 27.27, 26.25, 26.08, 25.99, 21.51, and 20.80. HRMS $[M - Br]^+$: calculated 845.4264, found 845.4262. **808-NM3** (0.50 g, yield 18%, HPLC purity analysis 99.5%). ^{1}H NMR (400 Hz, $CDCl_3$): 8.45 (s, 2H); 8.22 (d, J = 8.0 Hz, 2H); 7.62 (s, 1H); 7.61 (s, 1H); 7.47 (d, J = 8.0 Hz, 2H); 7.42 (t, J = 4.0 Hz, 2H); 7.28 (t, J = 4.0 Hz, 2H); 6.14 (d, J = 8.0 Hz, 2H); 4.24 (d, J = 4 Hz, 4H); 4.17 (d, J = 4 Hz, 4H); 2.59 (d, J = 4.0 Hz, 4H); 2.37 (s, 12H); 2.22−2.20 (m, 4H); 1.79−1.77 (m, 2H); and 1.67 (s, 12H). ^{13}C NMR (100 Hz, DMSO-d_6): 172.58, 148.63, 145.98, 145.57, 143.54, 142.30, 141.47, 129.05, 126.85, 125.72, 123.02, 122.25, 111.85, 101.97, 49.49, 44.25, 41.54, 27.90, 27.79, 26.25, 20.83, and 13.19. HRMS $[M - Br]^+$: calculated 789.3638, found 789.3661.

Cell Uptake and Subcellular Location. The cellular uptake of 808-NM2 was imaged and determined among MCF-10A, MCF-7, and 4T1 cells by laser confocal microscopy and flow cytometry analysis. All cells (5×10^5 cells/well) were seeded into six-well plates and cultured for 24 h. Cells were incubated in 1.25 μM 808-NM2 for 30 min and then stained with 4′,6-diamidino-2-phenylindole (DAPI) (Beyotime, Shanghai) for 10 min. After washing with phosphate-buffered saline (PBS) three times, cells were imaged using a Leica DMI6000 inverted microscope with a Leica TCS SP5 confocal scanning system (excitation: 808 nm channel). For flow cytometry analysis, the cells were trypsinized and collected with PBS. Cellular fluorescence was measured on a flow cytometer using an Accuir C6 flow cytometer (BD, Ann Arbor, MI). The cellular uptake of 808-NM2 was compared in MCF-7 and 4T1 cells in a normoxia chamber (21% O_2) with a CO_2 incubator (Thermo Fisher Scientific, CO_2 Incubator Steri-Cycle), a hypoxic chamber (5% O_2) with a tri-gas incubator (Thermo Fisher Scientific, CO_2 Incubator 3131) or an anaerobic incubator (Thermo Fisher Scientific, Forma 1029) under hypoxia (1% O_2), respectively. MCF-7 and 4T1 cells were seeded into six-well plates at a density of 5×10^5 cells/well in 2 mL complete medium and cultured at 37 °C for 24 h. Cells were incubated with 1.25 μM 808-NM2 for 30 min at 37 °C. After washing three times with PBS, cells were stained with DAPI for 10 min. Then, the cells were collected and washed three times with PBS. Cellular fluorescence was observed by laser confocal microscopy or measured by flow cytometry analysis. For subcellular localization, MCF-7 and 4T1 cells (5×10^5 cells/well) were seeded into six-well plates and cultured for 24 h. All cells were incubated with 1.25 μM 808-NM2 for 1 h, followed by MitoTracker Green (M7514) for 25 min. Then, the cells were fixed with 4% paraformaldehyde and stained with DAPI for 10 min in the dark. Finally, 1 mL 70% glycerinum was added to each well and imaged by confocal microscopy.

***In Vitro* Anticancer Effect.** The cytotoxicity of MCF-7 and 4T1 cells (3000 cells/well) was evaluated by a 3-(4,5-dimethylthiazol-2-yl)-2,5-diphenyltetrazolium bromide (MTT, M5655, Sigma-Aldrich) assay. MCF-7 and 4T1 cells were cultured with 100 μL of medium in 96-well plates and cultured for 24 h. Then, the cells were incubated with different concentrations of 808-NM2 for 72 h at 37 °C. The solution was discarded. Then, 20 μL of MTT solution (5 mg/mL) was added to each well and incubated for 4 h at 37 °C. The crystals were dissolved in 200 μL of DMSO, and the optical density (O.D.) was recorded at 490 nm. The cell viabilities of MCF-7 and 4T1 cells were compared under hypoxic and normoxic conditions during incubation with 808-NM2. MCF-7 and 4T1 cells (3×10^3 cells/well) were cultured with 100 μL of medium in 96-well plates for 24 h. The cells were cultured with different concentrations of 808-NM2 in a hypoxic chamber (5% O_2, 5% CO_2) or normoxia chamber (5% CO_2) for 24 h. The cell viabilities of MCF-7 and 4T1 cells were then tested by the MTT method as mentioned above. To observe multimodel anticancer activities, the cell viabilities of MCF-7 and 4T1 cells were determined after exposure to ionizing radiation under hypoxic and normoxic conditions. MCF-7 and 4T1 cells (3×10^3 cells/well) were cultured with 100 μL of medium in 96-well plates for 24 h. The cells were cultured with different concentrations of 808-NM2 in a hypoxic chamber (5% O_2, 5% CO_2) for 6 h. Then, the cells were treated with ionizing radiation (1 and 3 Gy) using RS2000 X-ray irradiator (RadSource Technologies) and incubated for 72 h. The cell viabilities were tested by MTT method as mentioned above.

Animals and Tumor Xenografts. Female BALB/c nude mice (4−6 weeks old) were purchased from the laboratory animal center of Third Military Medical University. All animal studies were approved by the Ethics Committee of the Third Military Medical University (Chongqing, China). For the tumor growth assay, nude mice were injected with 4T1 cells in 200 μL of serum-free RPMI-1640 medium at 2×10^5 cells/mouse in the left flank. Mice were randomized into three groups and treated with tail vein injection of normal saline or 10 mg/kg 808-NM2. The next day, for the 808-NM2 radiation group, only tumors were exposed to 4 Gy ionizing radiation with a lead cover. Small animal biological irradiator (Pxi X-RAD 320) was used for ionizing radiation treatment. Using a lead cover, only tumors were exposed to X-ray irradiation. Every other day, the mice were treated with 808-NM2 and irradiated three times. Tumor size was measured by calipers once every 2 days. On the 11th day after the first injection of 808-NM2, all of the tumors in the different groups were dissected from the mice and weighed. Lung organs were collected after mice were sacrificed at the end of observation. H&E staining or immunochemical staining of tumors or organs for pathological histology analysis was performed.

Patients-Derived Xenografts. Human samples were obtained from all patients with written informed consent. Both written informed consent and the study protocol were approved by the ethics committee of the First Affiliated Hospital of Army Medical University (namely, Southwest Hospital, Third Military Medical University, Approved No. KY2020002). Breast cancer fragments (0.5 cm) were obtained from the Department of Oncology, Southwest Hospital, Third Military Medical University and implanted in the left flanks of nude mice. Twenty days after tumor implantation, mice were divided into three groups: the control group, 808-NM2 (10 mg/kg) group, and 808-NM2 irradiation group (4 Gy). For the control and 808-NM2 groups, mice were injected with saline or 10 mg/kg 808-NM2, respectively. The next day, mice in the 808-NM2 radiation group were exposed to 4 Gy ionizing radiation. Every other day, the mice were treated with 808-NM2 and irradiated three times. Tumor size was measured by calipers once every 2 days. The mouse body weight was also recorded during treatment. On the 11th day after the first injection of 808-NM2, all tumors in the different groups were dissected from the mice and further stained for different kinds of immunohistochemistry analysis.

***In Vivo* NIR Imaging.** *In vivo* NIR imaging was performed using a small animal imaging system (Perkin Elmer, IVIS Spectrum). For the assessment of the tumor-targeting ability of 808-nitroimidazole conjugates, BALB/c mice bearing 4T1 xenografts were established and injected at a dose of 0.5 mg/kg by tail vein. *In vivo* NIR imaging was performed at different times after injection. After 24 h, mice were sacrificed, and the main organs, including tumors, were collected. *Ex vivo* NIR imaging was performed to observe their distribution. To assess the tumor-targeting ability in the PDX model, athymic nude mice were injected with 808-NM2 conjugates at a dose of 0.5 mg/kg via the tail vein. For comparison, the same protocols were performed, but nothing was implanted in mice as a sham-operated group.

Statistics Analysis. Data were reported as the mean and standard error of the mean (SEM) from at least three independent experiments; the p value was evaluated and calculated using a two-tailed paired t-test.

https://dx.doi.org/10.1021/acs.jmedchem.0c02250
J. Med. Chem. 2021, 64, 3381−3391

When there were multiple factors involved, a two-way analysis of variance (ANOVA) was used; multiple groups were compared using a one-way or two-way ANOVA. Values of $p < 0.05$ (* or #) were considered statistically significant.

■ ASSOCIATED CONTENT

Supporting Information

The Supporting Information is available free of charge at https://pubs.acs.org/doi/10.1021/acs.jmedchem.0c02250.

Additional experimental methods; synthetic route of 808-NM1, 808-NM2, and 808-NM3 (Figures S1 and S2); structural characterization of 808-NM2 (Figures S3 and S4); purity of final compounds (Figure S5); NIR optical determination (Figure S6); *in vitro* and *in vivo* tests on tumor growth inhibition (Figures S7−S23); physicochemical properties of 808-nitroimidazole conjugates (Table S1); and patient characteristics for the PDX model (Table S2) (PDF)

Molecular formula strings (CSV)

■ AUTHOR INFORMATION

Corresponding Authors

Changning Wang − *Department of Radiology, Athinoula A. Martinos Center for Biomedical Imaging, Massachusetts General Hospital, Harvard Medical School, Charlestown, Massachusetts 02129, United States;* orcid.org/0000-0002-2076-4193; Email: cwang15@mgh.harvard.edu

Shenglin Luo − *State Key Laboratory of Trauma, Burns and Combined Injury, Institute of Combined Injury, Chongqing Engineering Research Center for Nanomedicine, College of Preventive Medicine, Third Military Medical University (Army Medical University), Chongqing 400038, People's Republic of China;* orcid.org/0000-0002-0804-9891; Email: luosl@tmmu.edu.cn

Authors

Sha Chen − *State Key Laboratory of Trauma, Burns and Combined Injury, Institute of Combined Injury, Chongqing Engineering Research Center for Nanomedicine, College of Preventive Medicine and Department of Clinical Biochemistry, Laboratory Sciences, Third Military Medical University (Army Medical University), Chongqing 400038, People's Republic of China*

Songtao Yu − *Department of Oncology, Southwest Hospital, Third Military Medical University (Army Medical University), Chongqing 400038, People's Republic of China;* orcid.org/0000-0002-2804-9581

Zaizhi Du − *State Key Laboratory of Trauma, Burns and Combined Injury, Institute of Combined Injury, Chongqing Engineering Research Center for Nanomedicine, College of Preventive Medicine, Third Military Medical University (Army Medical University), Chongqing 400038, People's Republic of China*

Xie Huang − *State Key Laboratory of Trauma, Burns and Combined Injury, Institute of Combined Injury, Chongqing Engineering Research Center for Nanomedicine, College of Preventive Medicine, Third Military Medical University (Army Medical University), Chongqing 400038, People's Republic of China*

Meng He − *Department of Clinical Biochemistry, Laboratory Sciences, Third Military Medical University (Army Medical University), Chongqing 400038, People's Republic of China*

Shuang Long − *State Key Laboratory of Trauma, Burns and Combined Injury, Institute of Combined Injury, Chongqing Engineering Research Center for Nanomedicine, College of Preventive Medicine, Third Military Medical University (Army Medical University), Chongqing 400038, People's Republic of China*

Jing Liu − *State Key Laboratory of Trauma, Burns and Combined Injury, Institute of Combined Injury, Chongqing Engineering Research Center for Nanomedicine, College of Preventive Medicine, Third Military Medical University (Army Medical University), Chongqing 400038, People's Republic of China*

Yu Lan − *Department of Radiology, Athinoula A. Martinos Center for Biomedical Imaging, Massachusetts General Hospital, Harvard Medical School, Charlestown, Massachusetts 02129, United States*

Dong Yang − *Department of Radiology, Athinoula A. Martinos Center for Biomedical Imaging, Massachusetts General Hospital, Harvard Medical School, Charlestown, Massachusetts 02129, United States*

Hao Wang − *Department of Radiology, Athinoula A. Martinos Center for Biomedical Imaging, Massachusetts General Hospital, Harvard Medical School, Charlestown, Massachusetts 02129, United States*

Shuhui Li − *Department of Clinical Biochemistry, Laboratory Sciences, Third Military Medical University (Army Medical University), Chongqing 400038, People's Republic of China*

An Chen − *Department of Clinical Biochemistry, Laboratory Sciences, Third Military Medical University (Army Medical University), Chongqing 400038, People's Republic of China*

Yuhui Hao − *State Key Laboratory of Trauma, Burns and Combined Injury, Institute of Combined Injury, Chongqing Engineering Research Center for Nanomedicine, College of Preventive Medicine, Third Military Medical University (Army Medical University), Chongqing 400038, People's Republic of China*

Yongping Su − *State Key Laboratory of Trauma, Burns and Combined Injury, Institute of Combined Injury, Chongqing Engineering Research Center for Nanomedicine, College of Preventive Medicine, Third Military Medical University (Army Medical University), Chongqing 400038, People's Republic of China*

Complete contact information is available at: https://pubs.acs.org/10.1021/acs.jmedchem.0c02250

Author Contributions

⊥S.C. and S.Y. contributed equally to this work.

Notes

The authors declare no competing financial interest.

■ ACKNOWLEDGMENTS

The authors of this work acknowledge the financial support by National Natural Science Foundation of China (Nos. 81773352 and 81402784), Chongqing Youth Talent Project (CQYC2020058690), China Scholarship Council (No. 201703170071), Outstanding Youth Development Program in Third Military Medical University (No. 2017MPRC-17), and Intramural Research Project Grant (AEP17J001).

■ ABBREVIATIONS

BSP, sulfobromophthalein; 2-DG, 2-deoxy-D-glucose; mtDNA, mitochondrial DNA; NIR, near infrared; OATP, organic anion

transporting polypeptide; PET, positron emission tomography; PDX, patient-derived xenograft; ROS, reactive oxygen species; SPECT, single-photon emission computed tomography; VEGFR2, vascular endothelial growth factor receptor 2

REFERENCES

(1) Wilson, W. R.; Hay, M. P. Targeting hypoxia in cancer therapy. *Nat. Rev. Cancer* **2011**, *11*, 393−410.

(2) Barker, H. E.; Paget, J. T.; Khan, A. A.; Harrington, K. J. The tumour microenvironment after radiotherapy: mechanisms of resistance and recurrence. *Nat. Rev. Cancer* **2015**, *15*, 409−425.

(3) Pettersen, E.; Ebbesen, P.; Gieling, R.; Williams, K.; Dubois, L.; Lambin, P.; Ward, C.; Meehan, J.; Kunkler, I.; Langdon, S.; Ree, A.; Flatmark, K.; Lyng, H.; Calzada, M.; Peso, L.; Landazuri, M.; Görlach, A.; Flamm, H.; Kieninger, J.; Urban, G.; Weltin, A.; Singleton, D. C.; Haider, S.; Buffa, F. M.; Harris, A. L.; Scozzafava, A.; Supuran, C. T.; Moser, I.; Jobst, G.; Busk, M.; Toustrup, K.; Overgaard, J.; Alsner, J.; Pouyssegur, J.; Chiche, J.; Mazure, N.; Marchiq, I.; Parks, S.; Ahmed, A.; Ashcroft, M.; Pastorekova, S.; Cao, Y.; Rouschop, K. M.; Wouters, B. G.; Koritzinsky, M.; Mujcic, H.; Cojocari, D. Targeting tumour hypoxia to prevent cancer metastasis. From biology, biosensing and technology to drug development: the METOXIA consortium. *J. Enzyme Inhib. Med. Chem.* **2015**, *30*, 689−721.

(4) Forster, J. C.; Marcu, L. G.; Bezak, E. Approaches to combat hypoxia in cancer therapy and the potential for in silico models in their evaluation. *Phys. Med.* **2019**, *64*, 145−156.

(5) Jahanban-Esfahlan, R.; de la Guardia, M.; Ahmadi, D.; Yousefi, B. Modulating tumor hypoxia by nanomedicine for effective cancer therapy. *J. Cell. Physiol.* **2018**, *233*, 2019−2031.

(6) Ikeda, Y.; Hisano, H.; Nishikawa, Y.; Nagasaki, Y. Targeting and treatment of tumor hypoxia by newly designed prodrug possessing high permeability in solid tumors. *Mol. Pharm.* **2016**, *13*, 2283−2289.

(7) Liang, D.; Miller, G. H.; Tranmer, G. K. Hypoxia activated prodrugs:Factors influencing design and development. *Curr. Med. Chem.* **2015**, *22*, 4313−4325.

(8) Bonnet, M.; Hong, C. R.; Wong, W. W.; Liew, L. P.; Shome, A.; Wang, J.; Gu, Y.; Stevenson, R. J.; Qi, W.; Anderson, R. F.; Pruijn, F. B.; Wilson, W. R.; Jamieson, S. M. F.; Hicks, K. O.; Hay, M. P. Next-generation hypoxic cell radiosensitizers: nitroimidazole alkylsulfonamides. *J. Med. Chem.* **2018**, *61*, 1241−1254.

(9) Meißner, R.; Kocisek, J.; Feketeova, L.; Fedor, J.; Farnik, M.; Limao-Vieira, P.; Illenberger, E.; Denifl, S. Low-energy electrons transform the nimorazole molecule into a radiosensitiser. *Nat. Commun.* **2019**, *10*, No. 2388.

(10) Overgaard, J. Hypoxic Radiosensitization: adored and ignored. *J. Clin. Oncol.* **2007**, *25*, 4066−4074.

(11) Tan, X.; Luo, S.; Wang, D.; Su, Y.; Cheng, T.; Shi, C. A NIR heptamethine dye with intrinsic cancer targeting, imaging and photosensitizing properties. *Biomaterials* **2012**, *33*, 2230−2239.

(12) Shi, C.; Zhang, C.; Su, Y.; Cheng, T. Cyanine dyes in optical imaging of tumours. *Lancet Oncol.* **2010**, *11*, 815−816.

(13) Duan, L. L.; Wang, L.; Zhang, C.; Yu, L.; Guo, F.; Sun, Z.; Xu, Y.; Yan, F. Role of near-infrared heptamethine cyanine dye IR-783 in diagnosis of cervical cancer and its mechanism. *Int. J. Clin. Exp. Pathol.* **2019**, *12*, 2353−2362.

(14) Xiao, L.; Zhang, Y.; Yue, W.; Xie, X. Z.; Wang, J. P.; Chordia, M. D.; Chung, L. W. K.; Pan, D. F. Heptamethine cyanine based Cu-64-PET probe PC-1001 for cancer imaging: Synthesis and in vivo evaluation. *Nucl. Med. Biol.* **2013**, *40*, 351−360.

(15) Zhang, Y.; Xiao, L.; Popovic, K.; Xie, X. Z.; Chordia, M. D.; Chung, L. W. K.; Williams, M. B.; Yue, W.; Pan, D. F. Novel cancer-targeting SPECT/NIRF dual-modality imaging probe 99m Tc-PC-1007: Synthesis and biological evaluation. *Bioorg. Med. Chem. Lett.* **2013**, *23*, 6350−6354.

(16) Wu, J. B.; Lin, T. P.; Gallagher, J. D.; Kushal, S.; Chung, L. W. K.; Zhau, H. Y. E.; Oenyuk, B. Z.; Shih, J. C. Monoamine oxidase A inhibitor-near-infrared dye conjugate reduces prostate tumor growth. *J. Am. Chem. Soc.* **2015**, *137*, 2366−2374.

(17) Lv, Q. Z.; Yang, X. G.; Wang, M. L.; Yang, J. C.; Qin, Z. L.; Kan, Q. M.; Zhang, H. T.; Wang, Y. J.; Wang, D.; He, Z. G. Mitochondria-targeted prostate cancer therapy using a near-infrared fluorescence dye-monoamine oxidase A inhibitor conjugate. *J. Controlled Release* **2018**, *279*, 234−242.

(18) Luo, S.; Tan, X.; Fang, S. T.; Wang, Y.; Liu, T.; Wang, X.; Yuan, Y.; Sun, H. Q.; Qi, Q. R.; Shi, C. M. Mitochondria-targeted small-molecule fluorophores for dual modal cancer phototherapy. *Adv. Funct. Mater.* **2016**, *26*, 2826−2835.

(19) Tan, X.; Luo, S. L.; Long, L.; Wang, Y.; Wang, D. C.; Fang, S. T.; Ouyang, Q.; Su, Y. P.; Cheng, T. M.; Shi, C. M. Structure-guided design and synthesis of a mitochondria-targeting near-infrared fluorophore with multimodal therapeutic activities. *Adv. Mater.* **2017**, *29*, No. 1704196.

(20) Ntziachristos, V. Going deeper than microscopy: the optical imaging frontier in biology. *Nat. Methods* **2010**, *7*, 603−614.

(21) Guo, Q.; Luo, S.; Qi, Q.; Shi, C. Preliminary structure-activity relationship study of a couple of heptamethine indocyanine dyes for tumor-targeted imaging. *J. Innovative Opt. Health Sci.* **2013**, *6*, No. 1350003.

(22) Zhang, E.; Luo, S.; Tan, X.; Shi, C. Mechanistic study of IR-780 dye as a potential tumor targeting and drug delivery agent. *Biomaterials* **2014**, *35*, 771−778.

(23) Kroemer, G.; Reed, J. C. Mitochondrial control of cell death. *Nat. Med.* **2000**, *6*, 513−519.

(24) Wallace, D. C. Mitochondria and cancer. *Nat. Rev. Cancer* **2012**, *12*, 685−698.

(25) Shi, C. H.; Wu, J. B.; Chu, G. C. Y.; Li, Q. L.; Wang, R. X.; Zhang, C. Q.; Zhang, Y.; Kim, H. L.; Wang, J.; Zhau, H. Y. E.; Pan, D. F.; Chung, L. W. K. Heptamethine carbocyanine dye-mediated near-infrared imaging of canine and human cancers through the HIF-1 alpha/OATPs signaling axis. *Oncotarget* **2014**, *5*, 10114−10126.

(26) Wu, J. B.; Shao, C.; Li, X.; Shi, C.; Li, Q.; Hu, P.; Chen, Y.-T.; Dou, X.; Sahu, D.; Li, W.; Harada, H.; Zhang, Y.; Wang, R.; Zhau, H. E.; Chung, L. W. K. Near-infrared fluorescence imaging of cancer mediated by tumor hypoxia and HIF1α/OATPs signaling axis. *Biomaterials* **2014**, *35*, 8175−8185.

(27) Lee, W.; Belkhiri, A.; Lockhart, A. C.; Merchant, N.; Glaeser, H.; Harris, E. I.; Washington, M. K.; Brunt, E. M.; Zaika, A.; Kim, R. B.; El-Rifai, W. Overexpression of OATP1B3 confers apoptotic resistance in colon cancer. *Cancer Res.* **2008**, *68*, 10315−10323.

(28) Franken, N. A. P.; Rodermond, H. M.; Stap, J.; Haveman, J.; van Bree, C. Clonogenic assay of cells in vitro. *Nat. Protoc.* **2006**, *1*, 2315−2319.

(29) Yu, C. Y.; Xu, H.; Ji, S.; Kwok, R. T.; Lam, J. W.; Li, X.; Tang, B. Z.; et al. Mitochondrion-anchoring photosensitizer with aggregation-induced emission characteristics synergistically boosts the radiosensitivity of cancer cells to ionizing radiation. *Adv. Mater.* **2017**, *29*, No. 1606167.

(30) Baracca, A.; Sgarbi, G.; Solaini, G.; Lenaz, G. Rhodamine 123 as a probe of mitochondrial membrane potential: evaluation of proton flux through F0 during ATP synthesis. *Biochim. Biophys. Acta* **2003**, *1606*, 137−146.

(31) Ishikawa, K.; Takenaga, K.; Akimoto, M.; Koshikawa, N.; Yamaguchi, A.; Imanishi, H.; Nakada, K.; Honma, Y.; Hayashi, J. ROS-Generating mitochondrial DNA mutations can regulate tumor cell metastasis. *Science* **2008**, *320*, 661−664.

(32) Tuma, R. S. Making ROS for apoptosis. *J. Cell Biol.* **2005**, *170*, 513.

(33) Hoeben, A.; Landuyt, B.; Highley, M. S.; Wildiers, H.; Van Oosterom, A. T.; De Bruijn, E. A. Vascular endothelial growth factor and angiogenesis. *Pharmacol. Rev.* **2004**, *56*, 549−580.

(34) Guru, S. K.; Pathania, A. S.; Kumar, S.; Ramesh, D.; Vishwakarma, R. A.; Bhushan, S.; et al. Secalonic Acid-D Represses HIF1 alpha/VEGF-Mediated Angiogenesis by Regulating the Akt/mTOR/p70S6K Signaling Cascade. *Cancer Res.* **2015**, *75*, 2886−2896.

(35) Sullivan, H. C.; Edgar, M. A.; Cohen, C.; Kovach, C. K.; HooKim, K.; Reid, M. D. The utility of ERG, CD31 and CD34 in the cytological

https://dx.doi.org/10.1021/acs.jmedchem.0c02250
J. Med. Chem. 2021, 64, 3381−3391

diagnosis of angiosarcoma: an analysis of 25 cases. *J. Clin. Pathol.* **2015**, *68*, 44−50.

https://dx.doi.org/10.1021/acs.jmedchem.0c02250
J. Med. Chem. 2021, 64, 3381−3391